Journal of
Materials Chemistry A

ROYAL SOCIETY
OF CHEMISTRY

PAPER

View Article Online
View Journal | View Issue

Check for updates

Cite this: J. Mater. Chem. A, 2021, 9, 22585

MXene aerogel for efficient photothermally driven membrane distillation with dual-mode antimicrobial capability†

Sisi Cao,‡[a] Xuanhao Wu,‡[b] Yaguang Zhu,[b] Prashant Gupta,[a] Adrian Martinez,[b] Yunzhu Zhang,[b] Deoukchen Ghim,[b] Yixuan Wang,[a] Lin Liu,[a] Young-Shin Jun*[b] and Srikanth Singamaneni*[a]

Received 15th June 2021
Accepted 3rd September 2021

DOI: 10.1039/d1ta05058c

rsc.li/materials-a

Solar-driven desalination, which involves the conversion of solar energy to heat for freshwater generation, has been recognized as an attractive and sustainable desalination technology to alleviate freshwater shortage. In particular, photothermally driven membrane distillation (PMD) is a highly promising solar-driven desalination technology, especially in remote regions and disaster-struck communities, where no power infrastructure or waste heat from industrial plants is available. MXene, more specifically $Ti_3C_2T_x$, with excellent photothermal properties, easy processability, and electrical conductivity offers a great opportunity for realizing highly efficient, stable and multifunctional PMD membranes. Herein, we realize a MXene composite aerogel comprised of hydroxyapatite nanowires and poly(vinyl alcohol) with high thermal efficiency (61%) and water flux (0.72 kg m^{-2} h^{-1}) under 0.8 sun irradiation (0.8 kW m^{-2}), representing the first validation of highly efficient MXene-based PMD systems in treating ambient saline water. Owing to the strong interfacial interaction (*i.e.*, hydrogen bonding) between the building blocks, the MXene composite aerogel with high porosity (up to 91%) exhibited excellent mechanical stability. This highly interconnected porous network offers low resistance to vapor transport and low thermal conductivity, which minimizes conductive heat transfer across the aerogel, thus maximizing the thermal efficiency. Furthermore, the outstanding bactericidal activity induced by solar irradiation or electric potential makes the MXene composite aerogel a highly attractive candidate for PMD in the real world.

1. Introduction

To overcome the limited freshwater availability, increasing water demand and pollution caused by human activity, various desalination technologies have been developed to relieve the water scarcity, including reverse osmosis and thermal distillation.[1,2] However, there are still challenges to face for using these methods to address freshwater shortage because of their high energy consumption and high carbon footprint, especially for developing countries or rural areas where large power plants are not available.[3] To minimize the non-renewable energy consumption and reduce the possible adverse impacts on the environment during freshwater generation, emerging technologies, such as solar steam generation, are highly promising.[4–6] For solar stream generation, the advances in materials and the design of interfacial evaporators have promoted the thermal efficiency up to 90%, but the difficulty associated with freshwater collection from the generated vapor has still hindered their applications in the real world.[7] For instance, the reported thermal efficiency decreases by 60–70% after integrating the solar steam generator with the water collection system.[8,9] To address this challenge, another solar-driven desalination technology, photothermally driven membrane distillation (PMD), has been proposed, which integrates membrane distillation with the photothermal membrane.[10–13] Upon solar irradiation, surface heating is achieved on the photothermal membrane, and the vapor is generated at the interface between the feed water and the hydrophobic photothermal membrane. Driven by the vapor pressure caused by the temperature difference across the photothermal membrane, the vapor transports from the hot feed side to the cold permeate side of the photothermal membrane, where the vapor condenses for freshwater generation.

As a new series of 2D materials, the MXene family is composed of early transition metal carbides and/or carbonitrides, with a general formula of $M_{n+1}X_n$, where M represents a transition metal (*e.g.*, Sc, Ti, Zr, Hf, V, Nb, Ta, Cr, and Mo) and

---

[a] *Department of Mechanical Engineering and Materials Science, Institute of Materials Science and Engineering, Washington University in St. Louis, St. Louis, MO, 63130, USA. E-mail: singamaneni@wustl.edu*

[b] *Department of Energy, Environmental and Chemical Engineering, Washington University in St. Louis, St. Louis, MO, 63130, USA. E-mail: ysjun@wustl.edu*

† Electronic supplementary information (ESI) available. See DOI: 10.1039/d1ta05058c

‡ These authors contributed equally.

X is carbon and/or nitrogen.[14] Synthesized by wet-chemical etching using hydrofluoric (HF) acid or HF-containing or HF-forming etchants, functional groups (*e.g.*, –OH, –O and –F) are introduced on the surface of MXene,[15] and as-synthesized MXene is represented by $M_{n+1}X_nT_x$, where T_x refers to terminal functional groups.[16] Recently, MXene has been utilized in solar-driven desalination.[17] MXene exhibits broadband light absorption and an outstanding (∼100%) internal light-to-heat conversion efficiency, enabling excellent photothermal performance.[18] For instance, a MXene aerogel exhibited up to 96% light absorption.[19] Another attractive property of MXene is the high hydrophilicity due to the presence of hydroxyl groups, which precludes the need to use organic solvents during the membrane fabrication.[20] In addition, the abundant hydroxyl groups favor the interaction with other materials *via* hydrogen bonding to achieve the desired structure and enhanced mechanical properties.[21–24] Owing to these appealing properties, MXene has been processed into various forms, such as compact/porous films,[18,25–27] microspheres[28] and 3D aerogels,[21,29,30] and has been integrated with different materials to achieve high-performance solar evaporation.[25,31] Wang and co-workers have reported a compact MXene film integrated with a thermal insulator, exhibiting a thermal efficiency of 84% under 1 kW m^{-2} (1 sun).[18] A MXene aerogel with a tunable pore shape and size has been demonstrated for efficient solar evaporation with a thermal efficiency of 87% under 1 sun.[19] Although MXene-based solar evaporators exhibit high evaporation efficiency, freshwater generation efficiency significantly drops after integrating with the water collector. Thus, utilizing MXene in PMD membranes would unlock the full capability of MXene for more efficient resource use and effective clean water generation.

Chew and co-workers provided the first proof-of-concept of MXene in PMD and demonstrated that the flux of the MXene-coated polyvinylidene fluoride (PVDF) membrane was 10% higher under solar irradiation than that in the absence of solar light, when treating preheated saline water (65 °C).[32] However, the MXene-coated PVDF membrane exhibited a lower flux compared to the pristine PVDF membrane even under 5.8 sun light illumination. Such compromised performance in the presence of MXene results from the compact stacking structure of MXene, which greatly increases vapor transfer resistance. In addition, the compact MXene film possesses high thermal conductivity,[33,34] which leads to large conductive heat loss across the membrane during membrane distillation, consequently lowering its thermal efficiency. These issues highlight the need for optimizing the MXene architecture for an enhanced membrane distillation performance. The PMD performance of MXene in treating saline water at ambient temperature (*i.e.*, non-preheated) has not been investigated yet. The ability to implement PMD using non-preheated saline water is critical in remote regions and disaster-struck communities, where hot feed water is not readily available.[35] Yet another consideration in the utilization of MXene as a photothermal material is that MXene can be easily oxidized in the presence of water and oxygen.[36] Most of the previous reports indicate that MXene-based photothermal membranes can achieve stable evaporation performance,[37–39] but a recent report indicates the partial oxidation of MXene after solar steam generation.[30] Considering that the oxidation of MXene can lead to disintegration of the structure and deterioration of its photothermal performance, chemical stability of the MXene membrane is highly important for its long-term stable desalination performance.

Accounting for more than 45% of all membrane fouling, biofouling is responsible for a significant decline in water flux in various membrane distillation processes.[40–42] The addition of disinfectants and biocides has been suggested to overcome biofouling, but some of these chemical agents are toxic and induce negative effects on the environment. Physical cleaning, such as ultrasonication cleaning and back flushing, increases operational costs and may cause damage to the membrane. Recently, the photothermal effect and electric field have been proven as efficient and environment friendly methods to kill bacteria.[40,43–47] A photothermal membrane can kill bacteria effectively under sunlight irradiation owing to the photothermal effect, but it is not ideal when solar light is weak. As an alternative disinfection method, electric-field potential-driven disinfection can be achieved on a membrane possessing electric conductivity. Therefore, a membrane with excellent photothermal effect and electric conductivity properties is highly appealing to achieve versatile bactericidal capability.

Herein, we introduce a highly efficient and chemically stable MXene composite aerogel for PMD with dual-mode anti-biofouling capability. In the MXene composite aerogel, polyvinyl alcohol (PVA) is used as a binder material to improve the structural stability, and hydroxyapatite (HA) nanowires are added to lower the thermal conductivity of the aerogel, which in turn reduces the conductive heat loss.[35,48,49] The MXene composite aerogel, fabricated using ice-template assisted self-assembly, exhibits a highly interconnected porous network, allowing low resistance for vapor transfer. The high porosity (up to 91%) and low thermal conductivity (0.12 W m^{-1} K^{-1}) of the composite aerogel enable high thermal efficiency, up to 61%, in treating ambient temperature saline feedwater under 0.8 sun illumination (0.8 kW m^{-2}). We also demonstrate the outstanding bactericidal activity of the MXene composite aerogel both under solar irradiation and under external electric potential, thus obviating the need for harsh chemical/physical treatments for bacterial lysis. This work sheds light on the great potential of MXene in realizing a highly efficient, stable and biofouling-resistant photothermal membrane for high-performance PMD systems.

2. Results and discussion

2.1 Fabrication and characterization of the MXene/PVA/HA aerogel

A MXene composite aerogel was fabricated by integrating MXene flakes with PVA and HA nanowires (Fig. 1). $Ti_3C_2T_x$ MXene flakes were synthesized by selectively etching the Al layer from the Ti_3AlC_2 precursor using HCl/LiF followed by sonication to delaminate the multilayer $Ti_3C_2T_x$ MXene. The MXene flakes can be stably suspended in water, and the solution

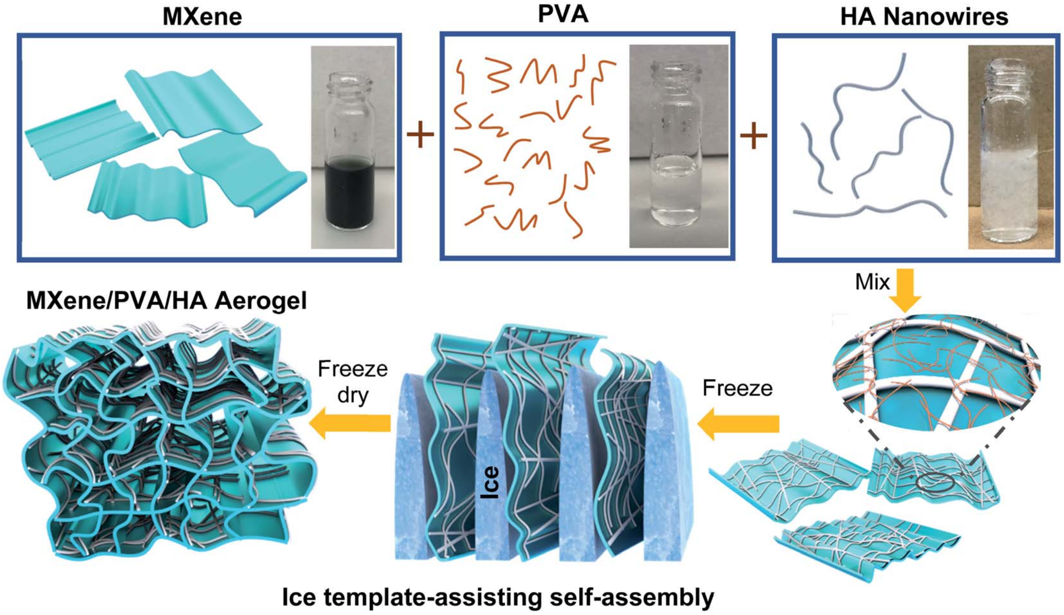

Fig. 1 Schematic illustration showing the fabrication of the MXene/PVA/HA aerogel using an ice template-mediated self-assembly method. Upon mixing with MXene flakes, PVA, and HA nanowires spontaneously wrap around the surface of MXene flakes. After freezing drying, the highly porous MXene composite aerogel is obtained.

appeared dark-green in color (Fig. 1). The scanning electron microscopy (SEM) image revealed well-exfoliated $Ti_3C_2T_x$ sheets (Fig. 2A), and the thickness measured using an atomic force microscope (AFM) was 2.7 nm (Fig. 2B). The successful preparation of $Ti_3C_2T_x$ was also confirmed by X-ray diffraction (XRD) analysis, showing the shift of the (002) peak to a lower 2θ angle, from 9.5° in Ti_3AlC_2 to 7.1° in $Ti_3C_2T_x$, which corresponded to a *d*-spacing shift from 9.2 Å to 12.4 Å (Fig. 2C).[16,50] The larger *d*-spacing in $Ti_3C_2T_x$ is ascribed to the introduction of terminal functional groups (*e.g.,* –OH, –O and –F) and incorporation of water molecules.[51] To fabricate the MXene composite aerogel, the $Ti_3C_2T_x$ colloid, PVA solution, and HA nanowire suspension were mixed. PVA is added as a binder material, and the addition of PVA is important. In the absence of PVA, the pristine MXene aerogel is too fragile to peel from the mold after freeze-drying. HA nanowires with outstanding flexibility were synthesized (Fig. S1†) by following a previous report using calcium oleate as a precursor *via* a hydrothermal method.[35] PVA and HA nanowires spontaneously adsorb on the MXene flakes owing to the abundant hydroxyl groups on each of these components, which facilitate hydrogen bonding. The PVA/HA-wrapped MXene flakes were assembled into a 3D porous aerogel structure by freezing-induced ice crystal templating (−20 °C) and subsequent freeze drying (Fig. 1).

The as-prepared black MXene/PVA/HA aerogel with a thickness of 400 μm (Fig. 2H) exhibited superior mechanical flexibility (Fig. 2D and G). SEM images (Fig. 2E, H and I) revealed a 3D interconnected microporous structure, and the porosity was measured to be 91%. Such high porosity offers low resistance for water transport during PMD and contributes to high thermal efficiency. Another important factor determining the thermal efficiency of a PMD membrane is its thermal conductivity. High thermal conductivity results in conductive heat transfer across the membrane and reduces the temperature difference across the photothermal membrane, leading to high resistance for vapor transport and thus low thermal efficiency. The $Ti_3C_2T_x$ has been reported to exhibit a relatively high thermal conductivity of 55.2 ± 1.7 W m^{-1} K^{-1}.[33] After incorporating HA nanowires with low thermal conductivity and realizing a stable aerogel structure with high porosity, the resultant composite aerogel exhibited a low thermal conductivity of 0.12 W m^{-1} K^{-1} (Fig. 3A and B). This low thermal conductivity enables efficient thermal insulation and high temperature difference across the aerogel during PMD, leading to high driving force for vapor transport.[52]

To realize efficient desalination during PMD, the photothermal membrane needs to be hydrophobic in order to prevent liquid phase transport and to ensure that only vapor can diffuse across the membrane. Owing to the abundant hydroxyl groups, the composite aerogel was completely hydrophilic with a water contact angle of 0°. After silanization using (tridecafluoro-1,1,2,2-tetrahydrooctyl)-trichlorosilane (FTCS), the contact angle of the MXene/PVA/HA aerogel increased to 138° (Fig. 3C), indicating successful surface hydrophobic functionalization. The SEM images showed that the highly porous network remained after this hydrophobic modification (Fig. S2A and B†).

2.2 Optical and photothermal properties

Considering that light absorption is critical for efficient photothermal performance, we investigated the light transmittance and reflectance of the composite aerogel (Fig. 3D and E). The PVA/HA aerogel (without MXene) exhibited high transmittance (~42%) and reflectance (~39%) in the visible region, implying relatively small light extinction (~19%). On the other hand, the MXene/

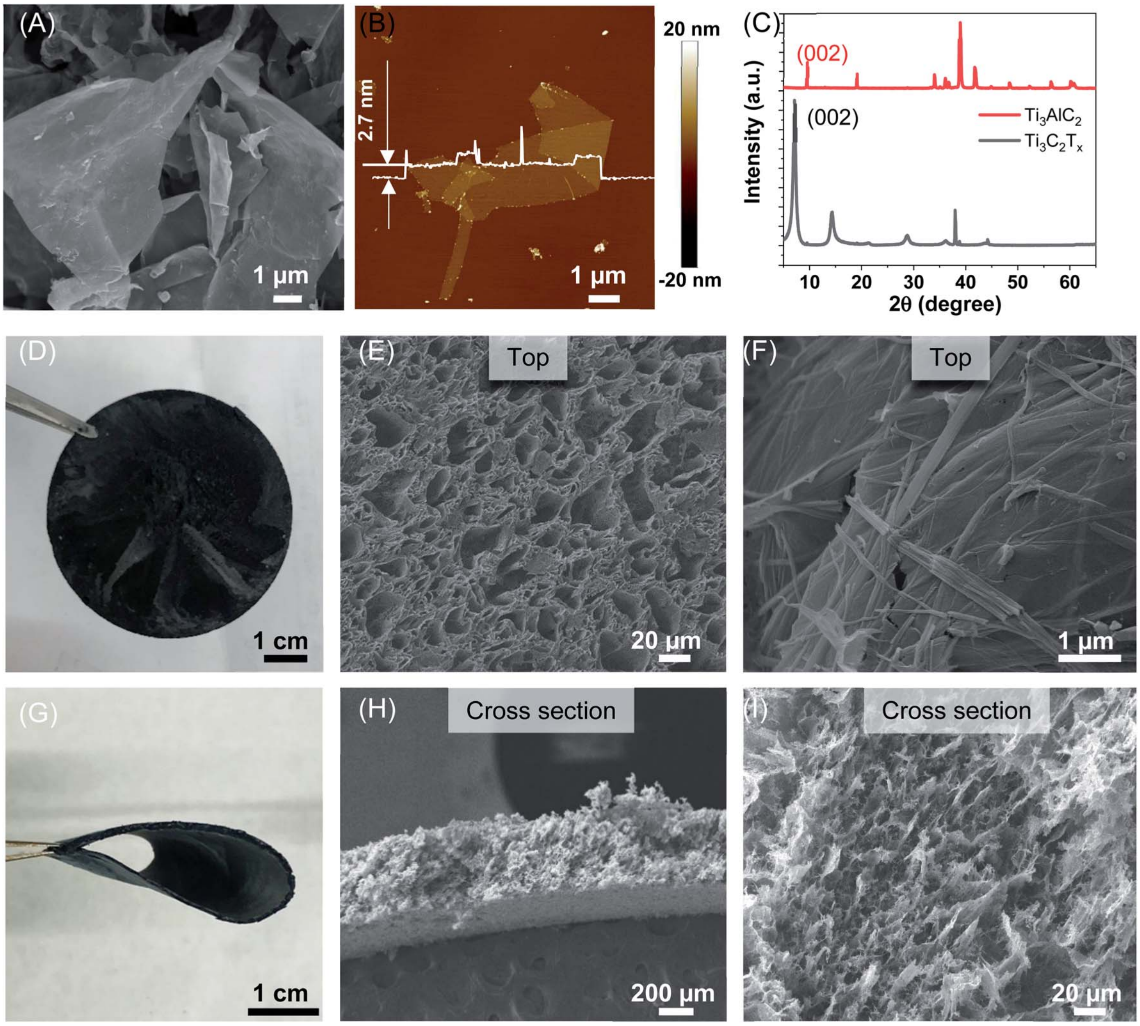

Fig. 2 (A) SEM and (B) AFM images of MXene flakes. (C) Comparison of XRD patterns of Ti_3AlC_2 and $Ti_3C_2T_x$. Photographs of (D) the as-prepared MXene/PVA/HA aerogel and (G) the bent MXene composite aerogel. SEM images of the top surface of the MXene composite aerogel at (E) low magnification and (F) high magnification. Cross-sectional SEM images of the MXene composite aerogel at (H) low magnification and (I) high magnification.

PVA/HA aerogel showed extremely low light transmittance (~2%) and reflectance (~1%), indicating a large light extinction (~97%). The large difference in the optical properties between the PVA/HA aerogel and MXene aerogel stems from the broadband light absorption of MXene.[25] In addition, the highly porous structure of the aerogel can result in multiple reflection when light travels through these pores and allows efficient light absorption.[31,53] Without the porous structure, a compact MXene film exhibited much higher light reflectance (~8%) (Fig. S3A and B†).

Next, we examined the photothermal performance of the MXene/PVA/HA aerogel and compared it with that of the PVA/HA aerogel. Previously reported PMD systems employ 0.7–1 sun irradiation to simulate daily sunlight irradiation,[43,54–67] so we test the photothermal performance of the aerogels under 0.8 sun. The surface temperature of these two aerogels in open air was monitored using an infrared camera, under simulated solar light illumination at a power density of 0.8 sun (Fig. 3F). After light irradiation for 180 seconds, the surface temperature of the PVA/HA aerogel increased from ~25 °C to ~32 °C (Fig. 3G), whereas the temperature of the MXene/PVA/HA aerogel increased to ~62 °C under identical irradiation conditions (Fig. 3H). The higher surface temperature realized on the MXene/PVA/HA aerogel, compared to the PVA/HA aerogel, highlights the outstanding light absorption and light-to-heat conversion enabled by MXene and its great potential in highly efficient PMD.

2.3 Photothermally driven membrane distillation

The PMD performance of MXene/PVA/HA was tested using an air gap membrane distillation (AMD) module (Fig. S4A and B†). The feed water was maintained to be the same as our reported test conditions, 0.5 M NaCl solution at ambient temperature (20 °C).[35,68,69] The feed water retention time can affect the PMD efficiency because of its effect on heat transfer and temperature polarization on the photothermal membrane.[12,68] Hence, different water retention times were tested (2 minutes, 3

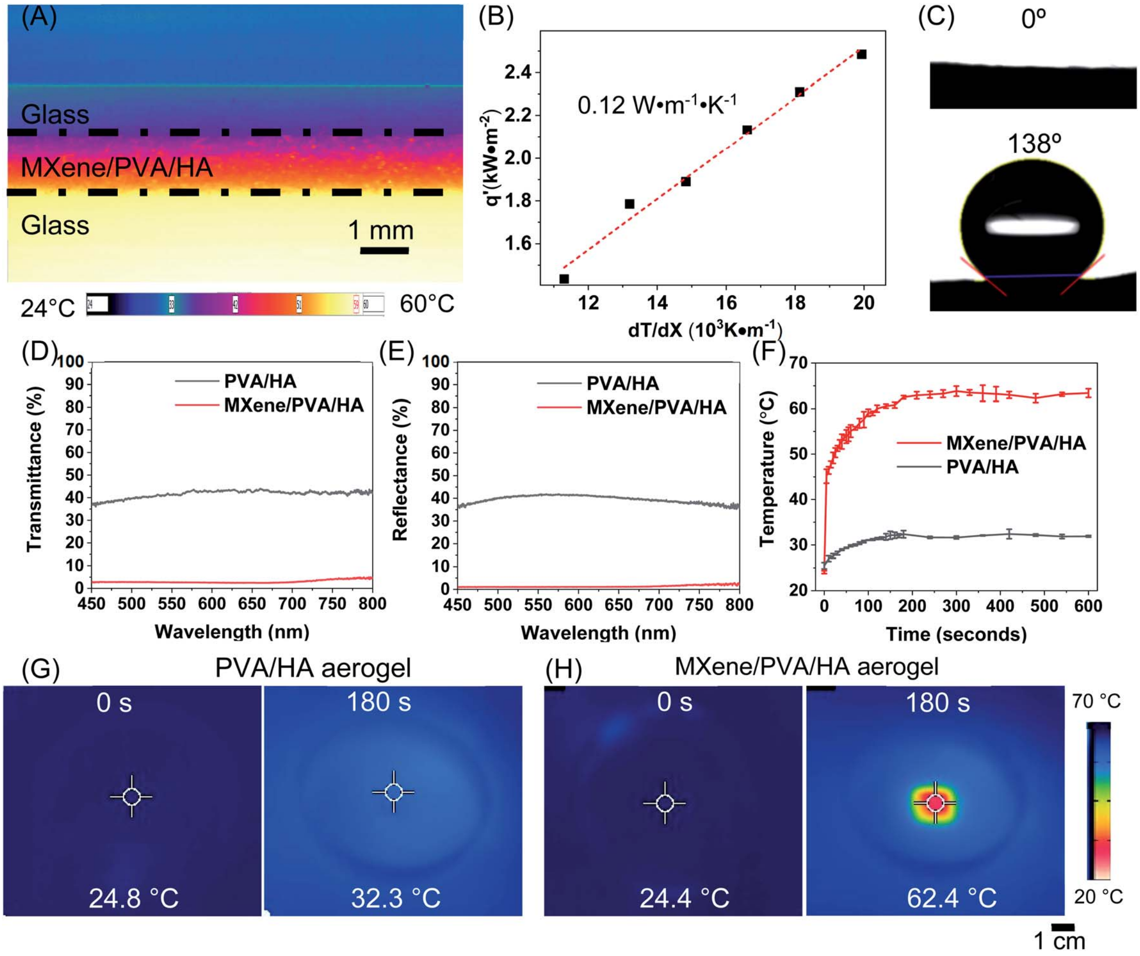

Fig. 3 (A) Infrared image showing the temperature gradient along the thickness of the composite aerogel. (B) Thermal conductivity of the MXene/PVA/HA aerogel. (C) Photograph showing the contact angle of the MXene/PVA/HA aerogel (top) and FTCS–MXene/PVA/HA aerogel (bottom). (D) Reflectance and (E) transmittance spectra of the PVA/HA aerogel and MXene/PVA/HA aerogel. (F) Plots showing the surface temperature of the PVA/HA aerogel and MXene/PVA/HA aerogel under simulated sunlight irradiation with a power density of 0.8 kW m^{-2} as a function of irradiation time. Infrared images showing the surface temperature of (G) the PVA/HA aerogel and (H) MXene/PVA/HA aerogel under simulated sunlight illumination with a power density of 0.8 kW m^{-2} in open air after 180 seconds.

minutes, and 5 minutes). After transporting through the photothermal membrane and air gap, the generated vapor finally condenses on a cold aluminum foil surface (Fig. 4A). The collected freshwater is quantified by measuring the weight increase of the distillate as a function of irradiation time (Fig. 4B). To evaluate the stability of PMD performance, the MXene composite aerogel was tested for over 5 cycles (each cycle for 1 hour). Under 0.8 sun illumination, the average water flux of the MXene/PVA/HA aerogel was 0.56 kg m^{-2} h^{-1}, 0.63 kg m^{-2} h^{-1} and 0.72 kg m^{-2} h^{-1} with a water retention time of 2 minutes, 3 minutes, and 5 minutes, respectively (Fig. 4C), and the variation in the flux within the same water retention time was less than 2%. The corresponding thermal efficiency of the MXene composite aerogel was calculated to be 48%, 54% and 61% for feed water retention times of 2 minutes, 3 minutes and 5 minutes, respectively (Fig. 4D).

The longer water retention time resulted in higher water flux and thermal efficiency. Under the same incident light, the longer retention time of feed water reduces the heat loss from the photothermal membrane to feed flow for more vapor generation,[12] and a larger temperature difference can also be achieved across the membrane for faster vapor transfer. The longer water retention time of feed water is also tested using static feed water. During a 1 hour test, the water flux was 0.84 kg m^{-2} h^{-1}, corresponding to a thermal efficiency of 72%. However, after uninterrupted 3 hour and 6 hour operation, the water flux reduced to 0.76 kg m^{-2} h^{-1} and 0.66 kg m^{-2} h^{-1} respectively. In the static feed water system, the salt concentration gradually increases with longer operation time, and high salt concentration of feed water leads to a decline in the water flux.[70] In addition, increasing the water retention time can also lead to a decline in water flux as the slow feed rate increases the salt fouling propensity, eventually blocking vapor transport channels.[2,71] Within the tested range of water retention times, high water flux can be obtained without salt accumulation on the composite aerogel when the water retention time of feed water is 5 minutes. However, further investigation needs to be conducted to determine the optimal water retention time.

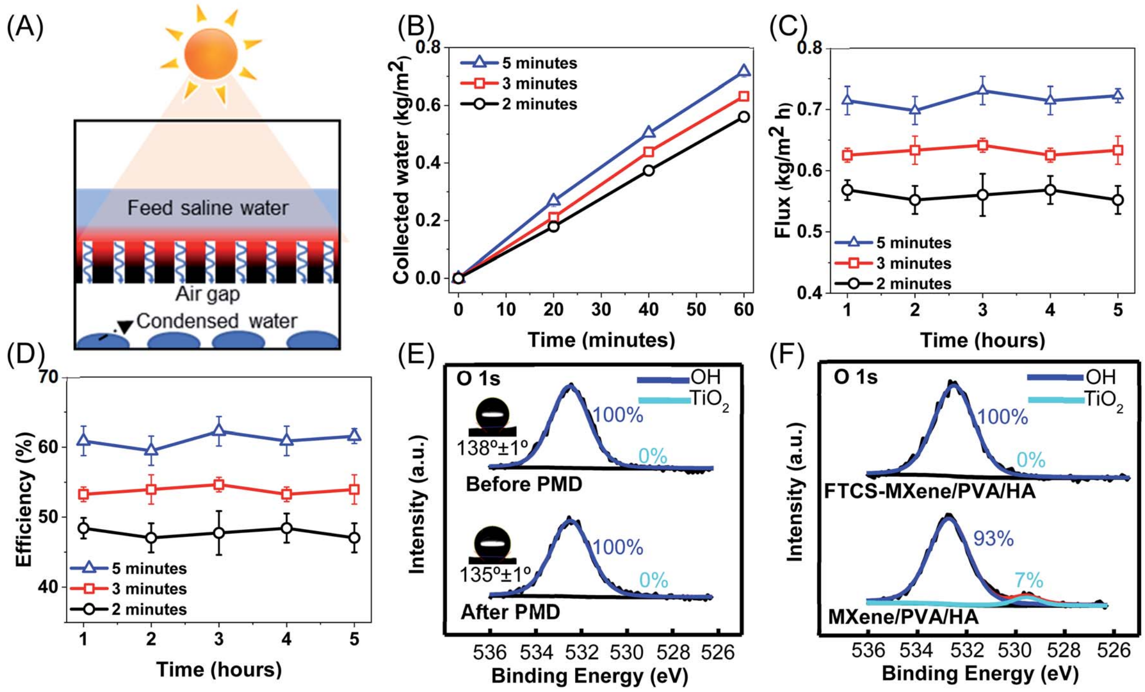

Fig. 4 (A) Schematic illustration of AMD using the FTCS–MXene/PVA/HA aerogel. (B) Collected water, (C) flux and (D) thermal efficiency of the PMD system using the FTCS–MXene/PVA/HA aerogel with varying feed water retention time, in purifying 0.5 M NaCl saline water under 0.8 sun irradiation over five consecutive cycles (each cycle for 1 hour, standard deviation obtained from measurements of 3 samples, error bars in (B) are smaller than the symbol size). (E) XPS of the FTCS–MXene/PVA/HA aerogel before and after the PMD test, insets show the contact angles of the aerogel before and after the PMD test. (F) Comparison of XPS of FTCS–MXene/PVA/HA and MXene/PVA/HA aerogels after subjecting to 0.5 M NaCl solution for 1 week.

The thermal efficiencies (48–61%) achieved on this MXene/PVA/HA aerogel are much higher than the previously reported PMD thermal efficiency realized by a PVDF-supported photothermal membrane in treating ambient saline water, including the carbon black nanoparticle-coated PVDF membrane (∼22%)[12] and polydopamine (PDA)-coated PVDF membrane (∼45%).[68] In addition, the FTCS–MXene/PVA/HA aerogel is comparable to the highly efficient photothermal membranes reported in PMD recently (Table S1†). The superior PMD performance stems from the high porosity of the composite aerogel. Because high porosity is critical for ensuring unimpeded vapor transfer,[52] the higher porosity of the MXene composite aerogel compared to previous PMD membranes enables the same. Specifically, the porosity of carbon black nanoparticle-coated and PDA-coated PVDF membranes was 65% and 75%, respectively, which are much lower than the porosity of the MXene composite aerogel (91%). Apart from low vapor transfer resistance, this MXene composite aerogel also exhibits optimal thermal management owing to its low thermal conductivity, which makes its overall thermal efficiency comparable to that of the recently reported high-performance bilayered photothermal membrane.[35,43] Furthermore, incorporation of materials with low thermal conductivity (*i.e.*, PVA and HA nanowires) suppresses the conductive heat transfer during PMD, facilitating a larger temperature difference across the aerogel and leading to a stronger driving force for fast vapor transport.

2.4 Stability of the FTCS–MXene/PVA/HA composite aerogel

The FTCS–MXene/PVA/HA aerogel exhibited stable performance for over a 5-cycle PMD test, and the variations in the thermal efficiency were less than 2% (Fig. 4D). To validate the long-term PMD performance, the FTCS–MXene/PVA/HA aerogel was subjected to an uninterrupted 12 hour PMD test. The total amount of collected water for the FTCS–MXene/PVA/HA aerogel was 4.5 g with a water retention time of 5 minutes, 3.9 g with a water retention time of 3 minutes, and 3.3 g with a water retention time of 2 minutes, corresponding to a water flux of $0.73\ \mathrm{kg\ m^{-2}\ h^{-1}}$, $0.63\ \mathrm{kg\ m^{-2}\ h^{-1}}$ and $0.53\ \mathrm{kg\ m^{-2}\ h^{-1}}$, respectively. The water flux under uninterrupted 12 hours of operation is similar to that of the cycling test, suggesting long-term stable performance and the salt rejection was around 99.98%. The Na^+ concentration of collected water was found to be within the range of 0.09 to 0.18 mM, which is far below the freshwater taste threshold defined by the World Health Organization (<11 mM).[72]

Even after vigorous mechanical agitation for 2 weeks, the FTCS–MXene/PVA/HA aerogel did not display any signs of disintegration (Fig. S5A†), and no change in morphology was observed (Fig. S5B†), highlighting the potential for long-term stability for PMD application. We then evaluated the chemical stability of the composite aerogel. The contact angle of FTCS-treated MXene/PVA/HA was 138° ± 1° and 135° ± 1° before and after a 5-cycle PMD test, respectively (Fig. 4E). The negligible change (variation less than 5%) in the contact angle of the aerogel indicated the robust surface modification and durable hydrophobicity for stable desalination. The chemical stability of MXene is important for long-term PMD performance. Based on previous studies, MXene can be easily oxidized into TiO_2 in the presence of oxygen and water,[37,73] resulting in the deterioration in photothermal performance. While MXene-based solar evaporators have been extensively investigated,[18,19,25,74] the chemical instability of MXene is still of significant concern in their translation to real-world applications. Thus, the chemical composition of FTCS-treated MXene before and after PMD performance was probed using XPS. The O 1s region revealed that the peak attributed to TiO_2 at a binding energy of 529.9 eV (ref. 75) was virtually absent before and after a 5-cycle PMD test, indicating the stable chemical structure of MXene over multiple cycles (Fig. 4E). Considering the easy oxidation of $Ti_3C_2T_x$ in the presence of water and air, we posit that the stability of $Ti_3C_2T_x$ stems from the FTCS treatment, which can prevent the direct contact of water with $Ti_3C_2T_x$. To validate this hypothesis, using the O 1s peak in XPS, we monitored and compared the chemical composition of MXene/PVA/HA and FTCS-treated MXene/PVA/HA aerogels after subjecting them to 0.5 M NaCl for 1 week (Fig. 4F). For the composite aerogel without FTCS, the oxygen peak associated with TiO_2 was discernible (with 7% area under the peak attributed to TiO_2), whereas no discernible TiO_2-associate oxygen peak was observed in the FTCS-treated aerogel. The excellent chemical stability of the FTCS-treated MXene/PVA/HA aerogel suggests that hydrophobic treatment is an effective method to prevent the oxidation of $Ti_3C_2T_x$. Current approaches to avoid the oxidation of $Ti_3C_2T_x$ involve freeze drying or the storage of $Ti_3C_2T_x$ colloids at low temperature (*e.g.*, aqueous solution at 4 °C) in an inert atmosphere to slow down the oxidation process. However, these approaches are not applicable for MXene-based solar evaporators. For the first time, our work first demonstrates the feasibility of realizing MXene-based 3D architectures with high chemical stability for long-term stable solar-driven desalination.

2.5 Dual-mode antibiofouling capability

To test the bactericidal ability, the FTCS-treated MXene aerogel was exposed to *E. coli* in the culture medium to induce the formation of a biofilm (Fig. 5A1). We have employed live/dead cell staining assay to quantify the bactericidal activity of the

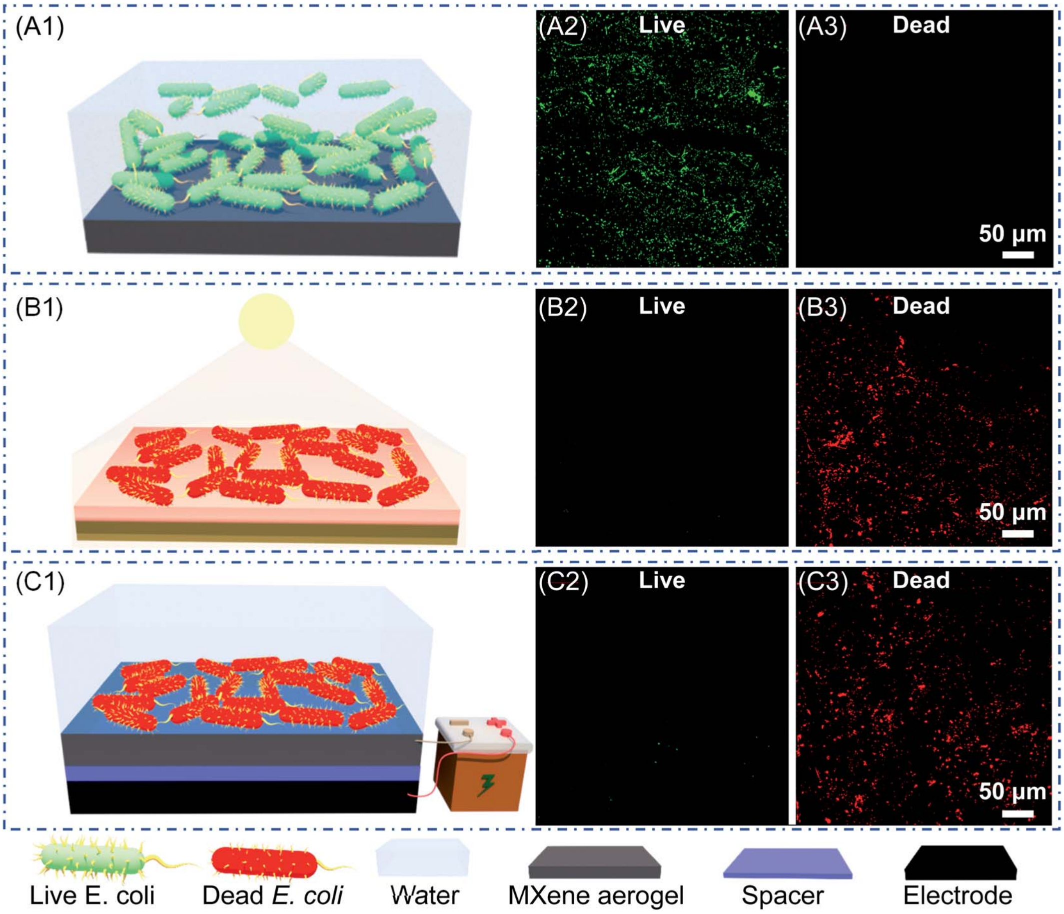

Fig. 5 (A1) Schematic illustration showing the accumulation of *E. coli* on the surface of the FTCS–MXene/PVA/HA aerogel after exposure to the culture medium contaminated with *E. coli* for 30 minutes. Schematic illustration of antibiofouling performance enabled by the FTCS–MXene/PVA/HA aerogel (B1) under solar irradiation in open air and (C1) after polarization with negative potential with a water thickness of 5 mm. Fluorescence images of *E. coli* on the surface of the FTCS–MXene/PVA/HA aerogel (A2 and A3) in pristine condition, (B2 and B3) under solar irradiation in open air for 10 minutes and (C2 and C3) after polarization with electric potential for 30 minutes.

aerogel. After 30 minute growth without light illumination, substantial green fluorescence was observed on the MXene composite aerogel (Fig. 5A2), suggesting the accumulation of live *E. coli* on the aerogel, and no signal of red fluorescence was noted (Fig. 5A3), indicating the absence of dead bacteria.

To test the anti-biofouling performance, the *E. coli* adhered MXene composite aerogel was either irradiated with solar light or subjected to electric potential. First, for testing photothermally driven anti-biofouling, we drained the *E. coli* culture medium, and the composite aerogel was irradiated with solar light with 0.8 sun for 10 minutes (Fig. 5B1). Only red fluorescence was observed, while the green fluorescence disappeared, revealing that solar irradiation was highly effective in killing the bacteria. It is known that bacteria become inactivated at temperatures above 55 °C after about five minutes.[76] Under sunlight irradiation, the surface temperature of the MXene composite aerogel reached up to 62 °C because of the photothermal effect, leading to effective disinfection by local surface heating.

To test electric field-induced anti-biofouling, the MXene composite aerogel was integrated with a spacer and an electrode, as indicated in Fig. 5C1. Then, negative voltage (-3.0 V) was applied on the MXene composite aerogel covered with *E. coli* culture medium for 30 minutes to test the *in situ* anti-biofouling performance. Following the application of the voltage, we noted that a relatively small fraction ($<1\%$) of the bacteria exhibited green fluorescence (Fig. 5C2), indicating live bacteria, while most of the bacteria exhibited red fluorescence (Fig. 5C3), corresponding to the dead bacteria. These fluorescence images of the MXene composite aerogel indicate that bacteria can be effectively killed when the composite aerogel is subjected to electric potential. MXene exhibits good conductivity,[77,78] and the electrical conductivity of the FTCS-treated MXene composite aerogel was measured to be 7.8 μS cm^{-1}. Considering that the charged surface can damage the cell membrane structure directly,[44,79] the MXene composite aerogel can offer effective disinfection after being polarized with external electric potential. This capability is particularly important because sunlight can be intermittent. Moderate voltages required for effective bactericidal activity can be easily achieved by solar powered batteries, avoiding the need for additional energy sources. This electric field-induced anti-biofouling performance serves as an alternative method for cost-effective disinfection when solar light is not adequate.

Next, we investigated the PMD performance of the FTCS–MXene/PVA/HA aerogel before and after disinfection. After immersion in the *E. coli* solution for 30 minutes, the FTCS–MXene/PVA/HA aerogel exhibited a water flux of 0.61 kg m^{-2} h^{-1} with a water retention time of 5 minutes under 0.8 sun irradiation for 30 minutes. Under identical test conditions, the water flux of the FTCS–MXene/PVA/HA aerogel was 0.71 kg m^{-2} h^{-1} and 0.70 kg m^{-2} h^{-1} after photothermal-driven disinfection and electric field-induced disinfection, respectively. The water flux of the FTCS–MXene/PVA/HA composite after disinfection was higher compared to before disinfection, highlighting the importance of anti-biofouling properties of the MXene composite aerogel in treating bacteria-contaminated water.

Therefore, based on the excellent photothermal effect and electric conductivity, this MXene composite aerogel shows versatile bactericide capability under solar irradiation or electric potential. Compared with chemical treatment or physical cleaning, the built-in anti-biofouling property of the MXene composite aerogel obviates the need for toxic chemicals or physical processes damaging the membrane, making the MXene aerogel highly appealing for treating bacteria-contaminated water.

3. Conclusion

In summary, we have successfully designed and fabricated an efficient and anti-biofouling MXene composite aerogel for highly efficient and stable PMD. The photothermal efficiency of the MXene/PVA/HA aerogel reached 61% under 0.8 sun illumination. This performance is superior to those of previously reported PVDF-supported photothermal membranes and comparable to those of recently reported thermally engineered photothermal membranes, in treating saline water at room temperature without any auxiliary heating system or heat recovery system. The as-prepared MXene/PVA/HA aerogel exhibited excellent photothermal performance owing to the broadband light absorption and high light-to-heat conversion efficiency of MXene. The high porosity and interconnected porous network created by an ice-templating method resulted in a low resistance to vapor transfer. Simultaneously, the composite aerogel exhibited low thermal conductivity, significantly reducing the conductive heat transfer from the evaporative surface to the cold permeate side and facilitating fast vapor transfer. FTCS-treatment minimized oxidation of MXene, providing excellent chemical stability to the MXene/PVA/HA aerogel even under prolonged exposure to saline water. Furthermore, due to the inherent photothermal properties and electrical conductivity, the MXene composite aerogel exhibited bactericidal activity under both solar irradiation and external electric potential. Owing to its high thermal efficiency, chemical stability and versatile bactericidal activity, the MXene composite aerogel is highly attractive for treating ambient saline water by utilizing the abundant sunlight, which is highly appealing for freshwater generation in remote regions and disaster-struck communities.

4. Experimental

4.1 Synthesis of $Ti_3C_2T_x$ MXene flakes

$Ti_3C_2T_x$ MXene flakes were synthesized by selectively etching the Al layer of Ti_3AlC_2 using LiF/HCl as previously reported.[16] Specifically, LiF (2 g, Alfa Aesar) was added to the HCl (9 M, 40 ml, Millipore Sigma) solution under stirring in a Teflon vessel to obtain a homogeneous solution. Then, Ti_3AlC_2 powder (1 g, Shanghai Chenyue Metal Co., Ltd, China) was slowly added to the LiF/HCl solution, and the mixture was transferred to an oil bath at 35 °C and left under stirring for 24 hours. The resultant suspension was centrifuged at 3500 rpm for 5 minutes. After decanting the supernatant, the collected product was dispersed in water. This wash step was repeated until the pH of the suspension was ~6. Finally, the suspension was subjected to sonication for 1 hour to delaminate the multilayer $Ti_3C_2T_x$ under Ar flow. After centrifuging at 3500 rpm for 1 hour, the $Ti_3C_2T_x$ flake colloid was obtained by collecting the supernatant. After bubbling Ar for 20 minutes, the collected $Ti_3C_2T_x$ colloid was stored at 4 °C in a sealed vial.

4.2 Fabrication of the MXene/PVA/HA aerogel and PVA/HA aerogel

HA nanowires were synthesized using the calcium oleate precursor *via* a solvothermal reaction reported previously.[35] After dispersing the PVA powder (M_w 8000–10 000, Millipore Sigma) in water, the mixture was kept in an oil bath at 60 °C for 2 hours under stirring to obtain a homogeneous solution. PVA solution (50 mg ml^{-1}, 0.5 ml) was added to the $Ti_3C_2T_x$ colloid (17 mg ml^{-1}, 0.5 ml). Then, the HA nanowire suspension (5 mg ml^{-1}, 1 ml) was added to the homogeneous mixture of $Ti_3C_2T_x$ and PVA. To fabricate the PVA/HA aerogel, the HA nanowire suspension (1 ml), the PVA solution (0.5 ml) and water (0.5 ml) were mixed homogeneously. To fabricate the aerogel, the mixture was transferred to a Petri dish with a diameter of 5.5 cm. After complete freezing at −20 °C, the mixture was freeze dried for 24 hours at −80 °C to obtain the aerogel.

4.3 Hydrophobic treatment

To convert the hydrophilic aerogel to the hydrophobic aerogel, the MXene/PVA/HA aerogel was treated with (tridecafluoro-1,1,2,2-tetrahydrooctyl) trichlorosilane (FTCS, Millipore Sigma) vapor in a sealed container at 70 °C for 24 hours. The water contact angle of the aerogel was measured using a contact angle analyzer (Phoenix 300, Surface Electro Optics Co. Ltd) to confirm the hydrophobicity after FTCS treatment.

4.4 Optical properties and photothermal performance

Reflectance and transmittance spectra of the aerogels were measured using a CRAIC micro spectrophotometer (QDI 302) coupled to a Leica optical microscope (DM 4000 M) with a 20× objective in the range of 450–800 nm with 10 accumulations and 100 milliseconds exposure time in reflection and transmission mode, respectively. The surface temperature of the aerogel with a size of 1 cm × 1 cm was monitored using an IR camera (FLIR E8-XT) under light illumination using a solar simulator (Newport 66921 Arc Lamp) with a light intensity of 0.8 kW m^{-2}, as measured using a spectroradiometer (SpectriLight ILT 950).

4.5 Thermal conductivity measurement

The thermal conductivities of the MXene/PVA/HA aerogel were measured by monitoring the temperature distribution across the thickness of the aerogel that was sandwiched between two glass microscope slides. The bottom glass slide was in contact with a hot plate and the top glass slide was in contact with ice. The temperature of the hot plate was increased from 70 °C to 120 °C, in steps of 10 °C. The vertical temperature distribution for the sandwich was monitored using a high-speed IR camera (Telops FAST M3k). The emissivity coefficient of a glass slide and a sample was assumed to be 0.9 to obtain the temperature distribution.[80] The Fourier equation was used to calculate the thermal conductivity of the aerogel:

$$q' = K\frac{\Delta T}{\Delta X}$$

The heat flux (q') was calculated by assuming a thermal conductivity (K) of 1.05 W m^{-1} K^{-1} for glass slides. Because the glass slide and samples experience the same heat flux, and the heat flux value obtained for the glass slide was used to measure the thermal conductivity of the MXene/PVA/HA aerogel.

4.6 Nano- and micro-structure characterization

Scanning electron microscopy (SEM) images of the surface and the cross-section of the aerogel and the nanowires were obtained after sputter coating the samples with gold. A FEI Nova 2300 field-emission SEM was used at an acceleration voltage of 10.5 kV. The atomic force microscopy (AFM) image was obtained using a Dimension 3000 (Bruker) in light tapping mode. A V-shaped silicon cantilever (Micromash) with a nominal tip radius of 8 nm was used for the imaging. The porosity was measured using isopropanol *via* a previously reported solvent replacement method.[43]

4.7 Chemical stability measurement

X-ray photoelectron spectroscopy (XPS, PHI 5000 VersaProbe II, Ulvac-PHI with monochromatic Al Kα radiation) was utilized to measure the O 1s spectra of MXene to understand chemical nature and changes in the chemical functionality of MXene. The contact angle and XPS of the FTCS-treated MXene/PVA/HA aerogel were monitored after a 5-cycle PMD test. To investigate the effect of hydrophobic treatment on the long-term stability, the pristine MXene/PVA/HA aerogel and FTCS-treated MXene/PVA/HA aerogel were immersed in 0.5 M NaCl solution for 1 week, respectively, and their chemical functionality was monitored and compared using XPS.

4.8 Photothermally driven membrane distillation performance measurement

The PMD performance was evaluated using an air gap membrane distillation (AMD) module. The PMD cell was constructed using the acrylonitrile butadiene styrene (ABS) plastic by 3D printing. The diameter of the MD cell was 3 cm, while the diameter of the membrane surface that was exposed to sunlight was measured to be 2.8 cm. The light illumination to AMD was achieved using a solar simulator under 0.8 sun illumination. NaCl aqueous solution (0.5 M) was employed as the feed water. The ambient feed water was continuously pumped using a peristaltic pump (model WPX1-F1/8S4-C, Welco Co. Ltd., Tokyo), with a flow rate of 1.57 ml min^{-1}, 1.06 ml min^{-1} and 0.62 ml min^{-1} to achieve a water retention time of 2 minutes, 3 minutes and 5 minutes, respectively. The thickness of the feed water was maintained at 5 mm. Aluminum foil was used as the condensation surface on the permeate side with a 2 mm air gap.

The amount of collected water was recorded using a weight scale (Sartorius ELT402).

The thermal efficiency of the photothermal membrane was determined by the ratio of heat flux required to generate distillate flux to the total irradiated solar flux,

$$\eta = \frac{mh_{\text{vap}}}{I}$$

where m represents the distillate flux of water, h_{vap} refers to the total evaporation enthalpy change, and I is the total incident solar flux. Given the water evaporation enthalpy of 2454 kJ kg^{-1} ($\sim$0.68 kW kg^{-1} h^{-1}), the thermal efficiency was calculated based on the input solar flux and distillate flux.

4.9 Antibiofouling test

To test the bactericidal activity, *E. coli* (pC013, Addgene) were cultured in Luria-Bertani (LB) liquid broth at 37 °C. All cultures were in 500 ml sterilized shake flasks (100 ml working volume, shaking at 250 rpm). After 12 hour culture, *E. coli* ($\sim$6.4 × 108 live cells per ml) were harvested. A layer of *E. coli* biofilm was formed on the surface of the FTCS-treated MXene/PVA/HA aerogel by exposing it to the feed solution comprised of LB medium with *E. coli* for 30 minutes. To test the photothermal disinfection ability, the feed solution was removed from the aerogel followed by 10 minute sunlight irradiation with a light intensity of 0.8 kW m^{-2}. To evaluate the bactericidal activity under electric potential, a two-electrode system consisting of a compact MXene film ($\sim$4 μm) and a polypropylene membrane as a spacer (3501 coated PP, Celgard LLC) was employed. The MXene film was fabricated by vacuum filtration of MXene colloids. The conductivity of the MXene composite aerogel was measured using a four-point conductivity cell (BT-110, Scribner Associates). Negative potential (−3.0 V) was applied on the aerogel for 30 minutes. The electrical potential was applied with a DC power supplier (Dr. Meter DC Power Supply HY3005D). The biofilm on the composite aerogel was monitored using fluorescent dyes (molecular probes live/dead bacterial cell viability kit, Thermo Fisher Scientific), and the fluorescence images were collected using a confocal laser scanning microscope (20× objective, Zeiss LSM 880 Laser Scanning Confocal Microscope) to identify the live bacteria and dead bacteria.

4.10 Mechanical agitation

Owing to the difficulty in conducting mechanical tests on the thin aerogel (*e.g.* compression test), the FTCS–MXene/PVA/HA aerogel was subjected to mechanical agitation to validate its mechanical stability. The aerogel (1 cm × 1 cm, $L \times W$) was placed in a 50 ml test tube filled with water, and then it was subjected to rigorous mechanical agitation in a tube rotator (VWR Multimix Tube Rotator Mixer 13916-822) for 2 weeks.

Conflicts of interest

There are no conflicts to declare.

Acknowledgements

We acknowledge the support from the National Science Foundation Environmental Engineering Program (CBET-1604542). The authors thank the Nano Research Facility (NRF) and Institute for Materials Science and Engineering (IMSE) at Washington University in St. Louis for providing access to characterization facilities.

References

1 Y.-S. Jun, X. Wu, D. Ghim, Q. Jiang, S. Cao and S. Singamaneni, *Acc. Chem. Res.*, 2019, **52**, 1215–1225.
2 A. Alkhudhiri, N. Darwish and N. Hilal, *Desalination*, 2012, **287**, 2–18.
3 C. Chen, Y. Kuang and L. Hu, *Joule*, 2019, **3**, 683–718.
4 S. Cao, P. Rathi, X. Wu, D. Ghim, Y.-S. Jun and S. Singamaneni, *Adv. Mater.*, 2021, **33**, 2000922.
5 D. Ghim, Q. Jiang, S. Cao, S. Singamaneni and Y.-S. Jun, *Nano Energy*, 2018, **53**, 949–957.
6 Y. Kuang, C. Chen, S. He, E. M. Hitz, Y. Wang, W. Gan, R. Mi and L. Hu, *Adv. Mater.*, 2019, **31**, 1900498.
7 S. Cao, Q. Jiang, X. Wu, D. Ghim, H. Gholami Derami, P.-I. Chou, Y.-S. Jun and S. Singamaneni, *J. Mater. Chem. A*, 2019, **7**, 24092–24123.
8 G. Ni, S. H. Zandavi, S. M. Javid, S. V. Boriskina, T. A. Cooper and G. Chen, *Energy Environ. Sci.*, 2018, **11**, 1510–1519.
9 L. Zhu, M. Gao, C. K. N. Peh, X. Wang and G. W. Ho, *Adv. Energy Mater.*, 2018, **8**, 1702149.
10 Y.-S. Jun, D. Ghim, X. Wu, S. Cao and S. Singamaneni, *HDIAC J.*, 2019, **6**, 6.
11 A. Politano, P. Argurio, G. Di Profio, V. Sanna, A. Cupolillo, S. Chakraborty, H. A. Arafat and E. Curcio, *Adv. Mater.*, 2017, **29**, 1603504.
12 P. D. Dongare, A. Alabastri, S. Pedersen, K. R. Zodrow, N. J. Hogan, O. Neumann, J. Wu, T. Wang, A. Deshmukh, M. Elimelech, Q. Li, P. Nordlander and N. J. Halas, *Proc. Natl. Acad. Sci. U. S. A.*, 2017, **114**, 6936–6941.
13 H. Gholami Derami, Q. Jiang, D. Ghim, S. Cao, Y. J. Chandar, J. J. Morrissey, Y.-S. Jun and S. Singamaneni, *ACS Appl. Nano Mater.*, 2019, **2**, 1092–1101.
14 B. Anasori, M. R. Lukatskaya and Y. Gogotsi, *Nat. Rev. Mater.*, 2017, **2**, 16098.
15 S. Hong, F. Ming, Y. Shi, R. Li, I. S. Kim, C. Y. Tang, H. N. Alshareef and P. Wang, *ACS Nano*, 2019, **13**, 8917–8925.
16 M. Alhabeb, K. Maleski, B. Anasori, P. Lelyukh, L. Clark, S. Sin and Y. Gogotsi, *Chem. Mater.*, 2017, **29**, 7633–7644.
17 Z. Xie, Y. Duo, Z. Lin, T. Fan, C. Xing, L. Yu, R. Wang, M. Qiu, Y. Zhang, Y. Zhao, X. Yan and H. Zhang, *Adv. Sci.*, 2020, **7**, 1902236.
18 R. Li, L. Zhang, L. Shi and P. Wang, *ACS Nano*, 2017, **11**, 3752–3759.
19 Q. Zhang, G. Yi, Z. Fu, H. Yu, S. Chen and X. Quan, *ACS Nano*, 2019, **13**, 13196–13207.
20 J. H. Kim, G. S. Park, Y.-J. Kim, E. Choi, J. Kang, O. Kwon, S. J. Kim, J. H. Cho and D. W. Kim, *ACS Nano*, 2021, **15**, 8860–8869.

21 X. Ming, A. Guo, Q. Zhang, Z. Guo, F. Yu, B. Hou, Y. Wang, K. P. Homewood and X. Wang, *Carbon*, 2020, **167**, 285–295.

22 J. Liu, H.-B. Zhang, X. Xie, R. Yang, Z. Liu, Y. Liu and Z.-Z. Yu, *Small*, 2018, **14**, 1802479.

23 M. C. Krecker, D. Bukharina, C. B. Hatter, Y. Gogotsi and V. V. Tsukruk, *Adv. Funct. Mater.*, 2020, **30**, 2004554.

24 D.-D. Shao, Q. Zhang, L. Wang, Z.-Y. Wang, Y.-X. Jing, X.-L. Cao, F. Zhang and S.-P. Sun, *J. Membr. Sci.*, 2021, **623**, 119033.

25 L. Tang, X. Zhao, C. Feng, L. Bai, J. Yang, R. Bao, Z. Liu, M. Yang and W. Yang, *Sol. Energy Mater. Sol. Cells*, 2019, **203**, 110174.

26 J. Zhao, Y. Yang, C. Yang, Y. Tian, Y. Han, J. Liu, X. Yin and W. Que, *J. Mater. Chem. A*, 2018, **6**, 16196–16204.

27 J. Liu, H.-B. Zhang, R. Sun, Y. Liu, Z. Liu, A. Zhou and Z.-Z. Yu, *Adv. Mater.*, 2017, **29**, 1702367.

28 X. Zhao, X.-J. Zha, L.-S. Tang, J.-H. Pu, K. Ke, R.-Y. Bao, Z.-y. Liu, M.-B. Yang and W. Yang, *Nano Res.*, 2020, **13**, 255–264.

29 X. Fan, Y. Yang, X. Shi, Y. Liu, H. Li, J. Liang and Y. Chen, *Adv. Funct. Mater.*, 2020, **30**, 2007110.

30 X. Zhao, L.-M. Peng, C.-Y. Tang, J.-H. Pu, X.-J. Zha, K. Ke, R.-Y. Bao, M.-B. Yang and W. Yang, *Mater. Horiz.*, 2020, **7**, 855–865.

31 K. Li, T.-H. Chang, Z. Li, H. Yang, F. Fu, T. Li, J. S. Ho and P.-Y. Chen, *Adv. Energy Mater.*, 2019, **9**, 1901687.

32 Y. Z. Tan, H. Wang, L. Han, M. B. Tanis-Kanbur, M. V. Pranav and J. W. Chew, *J. Membr. Sci.*, 2018, **565**, 254–265.

33 L. Chen, X. Shi, N. Yu, X. Zhang, X. Du and J. Lin, *Materials*, 2018, **11**, 1701.

34 H. Gholivand, S. Fuladi, Z. Hemmat, A. Salehi-Khojin and F. Khalili-Araghi, *J. Appl. Phys.*, 2019, **126**, 065101.

35 S. Cao, X. Wu, Y. Zhu, R. Gupta, A. Tan, Z. Wang, Y.-S. Jun and S. Singamaneni, *J. Mater. Chem. A*, 2020, **8**, 5147–5156.

36 Y. Lee, S. J. Kim, Y.-J. Kim, Y. Lim, Y. Chae, B.-J. Lee, Y.-T. Kim, H. Han, Y. Gogotsi and C. W. Ahn, *J. Mater. Chem. A*, 2020, **8**, 573–581.

37 Y. Chae, S. J. Kim, S.-Y. Cho, J. Choi, K. Maleski, B.-J. Lee, H.-T. Jung, Y. Gogotsi, Y. Lee and C. W. Ahn, *Nanoscale*, 2019, **11**, 8387–8393.

38 C. J. Zhang, S. Pinilla, N. McEvoy, C. P. Cullen, B. Anasori, E. Long, S.-H. Park, A. Seral-Ascaso, A. Shmeliov, D. Krishnan, C. Morant, X. Liu, G. S. Duesberg, Y. Gogotsi and V. Nicolosi, *Chem. Mater.*, 2017, **29**, 4848–4856.

39 F. Xia, J. Lao, R. Yu, X. Sang, J. Luo, Y. Li and J. Wu, *Nanoscale*, 2019, **11**, 23330–23337.

40 Q. Jiang, D. Ghim, S. Cao, S. Tadepalli, K.-K. Liu, H. Kwon, J. Luan, Y. Min, Y.-S. Jun and S. Singamaneni, *Environ. Sci. Technol.*, 2019, **53**, 412–421.

41 I. Luzinov, S. Minko and V. V. Tsukruk, *Prog. Polym. Sci.*, 2004, **29**, 635–698.

42 M. C. Vasudev, K. D. Anderson, T. J. Bunning, V. V. Tsukruk and R. R. Naik, *ACS Appl. Mater. Interfaces*, 2013, **5**, 3983–3994.

43 X. Wu, S. Cao, D. Ghim, Q. Jiang, S. Singamaneni and Y.-S. Jun, *Nano Energy*, 2021, **79**, 105353.

44 L. Jiang, L. Chen and L. Zhu, *Water Res.*, 2019, **161**, 297–307.

45 Y. Baek, H. Yoon, S. Shim, J. Choi and J. Yoon, *Environ. Sci. Technol. Lett.*, 2014, **1**, 179–184.

46 C.-F. de Lannoy, D. Jassby, K. Gloe, A. D. Gordon and M. R. Wiesner, *Environ. Sci. Technol.*, 2013, **47**, 2760–2768.

47 X.-J. Zha, X. Zhao, J.-H. Pu, L.-S. Tang, K. Ke, R.-Y. Bao, L. Bai, Z.-Y. Liu, M.-B. Yang and W. Yang, *ACS Appl. Mater. Interfaces*, 2019, **11**, 36589–36597.

48 D.-D. Qin, Y.-J. Zhu, F.-F. Chen, R.-L. Yang and Z.-C. Xiong, *Carbon*, 2019, **150**, 233–243.

49 Z.-C. Xiong, Y.-J. Zhu, D.-D. Qin, F.-F. Chen and R.-L. Yang, *Small*, 2018, **14**, 1803387.

50 G. Liu, J. Shen, Q. Liu, G. Liu, J. Xiong, J. Yang and W. Jin, *J. Membr. Sci.*, 2018, **548**, 548–558.

51 M.-Q. Zhao, X. Xie, C. E. Ren, T. Makaryan, B. Anasori, G. Wang and Y. Gogotsi, *Adv. Mater.*, 2017, **29**, 1702410.

52 D. Hou, T. Li, X. Chen, S. He, J. Dai, S. A. Mofid, D. Hou, A. Iddya, D. Jassby, R. Yang, L. Hu and Z. J. Ren, *Sci. Adv.*, 2019, **5**, eaaw3203.

53 P. Wang, *Environ. Sci.: Nano*, 2018, **5**, 1078–1089.

54 M. Fujiwara, *Desalination*, 2017, **404**, 79–86.

55 M. Fujiwara and M. Kikuchi, *Water Res.*, 2017, **127**, 96–103.

56 P. D. Dongare, A. Alabastri, S. Pedersen, K. R. Zodrow, N. J. Hogan, O. Neumann, J. Wu, T. Wang, A. Deshmukh and M. Elimelech, *Proc. Natl. Acad. Sci. U. S. A.*, 2017, **114**, 6936–6941.

57 X. Wu, Q. Jiang, D. Ghim, S. Singamaneni and Y.-S. Jun, *J. Mater. Chem. A*, 2018, **6**, 18799–18807.

58 L. Huang, J. Pei, H. Jiang and X. Hu, *Desalination*, 2018, **442**, 1–7.

59 Y. Z. Tan, H. Wang, L. Han, M. B. Tanis-Kanbur, M. V. Pranav and J. W. Chew, *J. Membr. Sci.*, 2018, **565**, 254–265.

60 Y. Tian, M. Zhou, H. Shi, S. Gao, G. Xie, M. Zhu, M. Wu, J. Chen and Z. Niu, *Nano Lett.*, 2018, **18**, 5453–5460.

61 B. Gong, H. Yang, S. Wu, J. Yan, K. Cen, Z. Bo and K. K. Ostrikov, *ACS Sustainable Chem. Eng.*, 2019, **7**, 20151–20158.

62 B. Gong, H. Yang, S. Wu, G. Xiong, J. Yan, K. Cen, Z. Bo and K. Ostrikov, *Nano-Micro Lett.*, 2019, **11**, 51.

63 X. Han, W. Wang, K. Zuo, L. Chen, L. Yuan, J. Liang, Q. Li, P. M. Ajayan, Y. Zhao and J. Lou, *Nano Energy*, 2019, **60**, 567–575.

64 S. Cao, X. Wu, Y. Zhu, R. Gupta, A. Tan, Z. Wang, Y.-S. Jun and S. Singamaneni, *J. Mater. Chem. A*, 2020, **8**, 5147–5156.

65 J. Huang, Y. Hu, Y. Bai, Y. He and J. Zhu, *Desalination*, 2020, **489**, 114529.

66 W. Li, Y. Chen, L. Yao, X. Ren, Y. Li and L. Deng, *Desalination*, 2020, **478**, 114288.

67 Y. Zhang, K. Li, L. Liu, K. Wang, J. Xiang, D. Hou and J. Wang, *Chemosphere*, 2020, 127053.

68 X. Wu, Q. Jiang, D. Ghim, S. Singamaneni and Y.-S. Jun, *J. Mater. Chem. A*, 2018, **6**, 18799–18807.

69 X. Wu, S. Cao, D. Ghim, Q. Jiang, S. Singamaneni and Y.-S. Jun, *Nano Energy*, 2020, 105353.

70 Y. Peng, Y. Wang, W. Li and J. Jin, *J. Mater. Chem. A*, 2021, **9**, 10678–10684.

71 M. Gryta, *J. Membr. Sci.*, 2008, **325**, 383–394.

72 P. Zhang, Q. Liao, H. Yao, Y. Huang, H. Cheng and L. Qu, *Energy Storage Mater.*, 2019, **18**, 429–446.
73 T. Habib, X. Zhao, S. A. Shah, Y. Chen, W. Sun, H. An, J. L. Lutkenhaus, M. Radovic and M. J. Green, *npj 2D Mater. Appl.*, 2019, **3**, 8.
74 X. Zhao, X.-J. Zha, J.-H. Pu, L. Bai, R.-Y. Bao, Z.-Y. Liu, M.-B. Yang and W. Yang, *J. Mater. Chem. A*, 2019, **7**, 10446–10455.
75 J. Halim, K. M. Cook, M. Naguib, P. Eklund, Y. Gogotsi, J. Rosen and M. W. Barsoum, *Appl. Surf. Sci.*, 2016, **362**, 406–417.
76 A. T. Spinks, R. H. Dunstan, T. Harrison, P. Coombes and G. Kuczera, *Water Res.*, 2006, **40**, 1326–1332.
77 Z. Wu, T. Shang, Y. Deng, Y. Tao and Q.-H. Yang, *Adv. Sci.*, 2020, **7**, 1903077.
78 Z. Wang, S. Kang, S. Cao, M. Krecker, V. V. Tsukruk and S. Singamaneni, *MRS Bull.*, 2020, **45**, 1017–1026.
79 V. R. Krishnamurthi, A. Rogers, J. Peifer, I. Niyonshuti, J. Chen and Y. Wang, *Appl. Environ. Microbiol.*, 2020, **86**, e01015–01020.
80 Q. Jiang, L. Tian, K.-K. Liu, S. Tadepalli, R. Raliya, P. Biswas, R. R. Naik and S. Singamaneni, *Adv. Mater.*, 2016, **28**, 9400–9407.